





# Understanding the magnetic dynamics and magnetostructural coupling in the paramagnetic phase of TbMnO<sub>3</sub> by muon-spin spectroscopy

R. Vilarinho <sup>1,\*</sup>, R. C. Vilão,<sup>2</sup> H. V. Alberto,<sup>2</sup> A. G. Marinopoulos <sup>2</sup>, J. M. Gil,<sup>2</sup> H. Luetkens,<sup>3</sup> Z. Guguchia,<sup>3</sup> M. Mihalik <sup>4</sup>, M. Mihalik, Jr.,<sup>4</sup> and J. Agostinho Moreira <sup>1</sup>

<sup>1</sup>IFIMUP, Departamento de Física e Astronomia, Faculdade de Ciências da Universidade do Porto, 4169-007, Porto, Portugal

<sup>2</sup>CFisUC, Department of Physics, University of Coimbra, R. Larga, Coimbra, 3004–516, Portugal

<sup>3</sup>Paul Scherrer Institute (PSI), 5232 Villigen, Switzerland

<sup>4</sup>Institute of Experimental Physics Slovak Academy of Sciences, Watsonova 47, Košice, Slovak Republic



(Received 22 May 2023; accepted 18 October 2023; published 1 November 2023)

In this work we present a comprehensive study of the spin dynamics and fluctuations in the ordered magnetic phases of the prototype multiferroic material TbMnO<sub>3</sub>. From the temperature dependence of the dynamical and static components of the time-dependent asymmetry, we demonstrate the existence of strong local magnetic-field disorder arising from the modulated Mn<sup>3+</sup> spin arrangement and the effect of the Tb<sup>3+</sup> ordering at low temperatures. We provide evidence for an unusual magnetostructural coupling in the paramagnetic phase of TbMnO<sub>3</sub> by means of muon spin spectroscopy. No short-range magnetic ordering definitively occurs in the paramagnetic phase and the unusual properties found in the temperature dependence of the magnetic susceptibility are due to a magnetostructural coupling, likely involving oxygen displacements.

DOI: [10.1103/PhysRevB.108.174401](https://doi.org/10.1103/PhysRevB.108.174401)

## I. INTRODUCTION

TbMnO<sub>3</sub> has found a special position in the condensed-matter research field because it exhibits intrinsic magnetoelectric multiferroic phases at low temperatures [1–5]. TbMnO<sub>3</sub> crystallizes at room conditions in the orthorhombic *Pbnm* structure [5]. The Mn<sup>3+</sup> cations are in an octahedral oxygen environment, while the Tb<sup>3+</sup> ions occupy a distorted oxygen dodecahedra. Due to both the octahedra tilting and the Jahn-Teller activity of the Mn<sup>3+</sup> cations in the high-spin configuration, the oxygen polyhedra are distorted. At  $T_N = 41$  K, the Mn<sup>3+</sup> spins order in a collinear sinusoidal incommensurate modulated antiferromagnetic structure, with the modulation running along the *b* axis [4]. On further cooling, the modulation wave vector continuously decreases and at  $T_c = 28$  K, a second antiferromagnetic phase transition takes place into a modulated cycloidal spiral antiferromagnetic spin ordering in the *bc* plane, developing along the *b* axis [6]. This antiferromagnetic structure allows for ferroelectricity, with spontaneous polarization along the *c* axis, which is well described by the Dzyaloshinskii-Moriya model [4]. The electric polarization flips from the *c* axis to the *a* axis when a magnetic field ( $B > 5$  T) is applied along the *b* axis, due to the rotation of the spin cycloid from the *bc*- to the *ab* plane [4]. The Tb<sup>3+</sup> spins align antiferromagnetically below  $T_{N2} = 7$  K in a quasi-long-range ordering [5].

Although the low-temperature phase sequence has been extensively studied, the spin dynamics, local magnetic-field distribution, and magnetic disorder arising from the different Mn<sup>3+</sup> spin structures and the Tb<sup>3+</sup> spin ordering have not

been properly addressed. Furthermore, intriguing abnormal features in the temperature dependence of structural, magnetic, and thermal properties of TbMnO<sub>3</sub> have been reported in the paramagnetic phase, well above  $T_N$ . These include the deviation from the Curie-Weiss law of the magnetic susceptibility along the *b* axis below 200 K [7,8], and the anomalous temperature behavior of optical phonons [8], thermal conductivity [9], lattice parameters [10], and elastic moduli [11] in the 90 to 200 K range. Moreover, the  $E^\omega \parallel a$ -polarized THz absorption spectra exhibit a broad and weak band at around 20 cm<sup>-1</sup>, at room temperature, whose intensity gradually increases on cooling from 150 K, while the oscillator strength of the lowest-lying optical polar phonon concomitantly decreases [12]. This temperature evolution does not follow the expected behavior of a usual paramagnetic insulating phase.

Two controversial interpretations have been proposed. The anomalous temperature dependence of the thermal conductivity coefficients has been interpreted as a resonant-scattering process of phonons between different energy levels of the 4*f* Tb<sup>3+</sup> multiplets, where the Mn<sup>3+</sup> magnetism plays a minor role [8,9]. The temperature anomalies of lattice phonons, studied by polarized Fourier transform infrared spectroscopy and Raman scattering, have been attributed to local displacements of the oxygen atoms, as a result of the crystal-field energy level shifts below 120 K [8,12]. Another picture is based on short-range magnetic clusters established in the paramagnetic phase, below 150 K, which would explain the deviation of the magnetic susceptibility from the Curie-Weiss law and the observation of bands in the THz absorption spectra assigned to electromagnons [13].

More recently, low-field temperature-dependent muon spin resonance experiments in TbMnO<sub>3</sub> ceramic samples were carried out in order to get information about the local changes

\*rvsilva@fc.up.pt

which underly the anomalous temperature dependence observed in many physical quantities in the paramagnetic phase, as referred to above, and the magnetic-field distribution in the ordered phases, as well [14]. The  $\mu$ SR time signal recorded at different temperatures in the range  $T_N < T < 150$  K exhibits two distinct relaxing components with anomalously high relaxation. The temperature dependence of the asymmetries associated with the two relaxing components and their low magnetic-field dependence was interpreted as a coexistence of two states in the  $T_N < T < 150$  K range. These features have been ascribed to the existence of noninteracting isolated magnetic regions, with a magnetic ordering, within the paramagnetic matrix [14].

The previous  $\mu$ SR measurements in  $\text{TbMnO}_3$  ceramic samples have been rather limited, particularly in the time resolution of the spectrometer used, and no accurate information regarding internal fields could be assessed in the magnetic ordered phases below  $T_N$ . In order to characterize the dynamic and static local magnetic-field distributions due to the  $\text{Mn}^{3+}$  and  $\text{Tb}^{3+}$  spin order and to get a definitive answer on the mechanisms underlying the abnormal features observed in the paramagnetic phase, we performed  $\mu$ SR experiments using  $\text{TbMnO}_3$ -oriented single-crystalline samples, with a twofold objective: to characterize the local field distribution and its temperature dependence for the ordered magnetic phases by temperature-dependent zero-field measurements, and to study the local magnetic field at the  $\mu$  sites by an analysis of the Knight shift as a function of temperature and applied transversal magnetic field, focusing on the paramagnetic phase. The present study also reports first-principles calculations, based on density-functional theory (DFT) [15,16] that aimed to determine all possible muon-stopping sites. We anticipate that our results will definitively present a view of local magnetism and answer fundamental questions regarding the macroscopic features of  $\text{TbMnO}_3$  in a broad temperature range.

## II. EXPERIMENTAL DETAILS

High-quality  $\text{TbMnO}_3$  single crystals were grown by floating-zone method in an FZ-T-4000 (Crystal Systems Corporation) mirror furnace, using  $\text{Tb}_4\text{O}_7$  and  $\text{Fe}_2\text{O}_3$  as starting materials. The starting materials were mixed in the stoichiometric ratio, cold pressed into rods, and sintered at 1100 °C for 12–14 h in air. Growing was performed in air atmosphere; feed and seed rod were rotated with a speed of 30 rpm in opposite directions and a pulling speed of 6 mm/h was used. The typical length of a grown ingot was between 3 and 5 cm [17,18].

The  $Pbnm$  phase and single-crystalline character of the used samples were previously confirmed by room-temperature x-ray diffraction and Raman spectroscopy. No spurious phases could be detected. The quality of the samples was also confirmed by the critical temperature values; ascertained from the temperatures was that the specific-heat and the magnetization data exhibit anomalies (see Fig. S1 of Supplemental Material [19]). The results obtained are found to agree with those reported earlier for  $\text{TbMnO}_3$  [7].

Muon-spin spectroscopy measurements were performed on the oriented  $\text{TbMnO}_3$  single-crystalline samples, at the Swiss Muon Source ( $S\mu S$ ) of the Paul Scherrer Institute (PSI).

Zero-field measurements were undertaken at the GPS instrument at fixed temperatures between 2 and 50 K. Measurements with a applied high magnetic field in transverse geometry were performed at the HAL-9500 instrument in the temperature range 10 to 300 K. Muons with 100% spin polarization and a kinetic energy of 4 MeV were implanted in the crystals, with the spin polarization parallel to the  $c$  axis in both experiments; in the transverse geometry measurements, the magnetic field was applied along the  $b$  axis (i.e., the  $\text{Mn}^{3+}$  spin modulation direction). The time evolution of the muon spin polarization was determined from the asymmetry of the decay positrons and analyzed with the WIMDA and MUSRFIT software [20,21].

First-principles calculations were performed using the VASP code [22–24]. These are based on spin-polarized DFT with additional Hubbard-type interactions for the on-site correlations between the manganese  $3d$  electrons [25]. A value of  $U$  for the on-site potential equal to 2.0 eV was used, in agreement with earlier DFT+ $U$  studies of the  $\text{TbMnO}_3$  compound [26–28]. The core-valence interactions were described by pseudopotentials that were constructed within the projector augmented-wave method [29]. For  $\text{Mn}^{3+}$  the  $3p$  states were treated as valence states together with the  $3d$  and  $4s$  electrons, while the  $4f$  electrons of Tb were assumed to be core states. The semilocal Perdew-Burke-Ernzerhof functional based on the generalized-gradient approximation was employed for treating the exchange and correlation effects between the electrons [30]. The valence crystalline wave functions were expanded in a plane-wave basis limited by an energy cutoff of 420 eV. Muons were represented by the positively charged interstitial  $\text{H}^+$  nuclei, since both of these particles are expected to have almost identical ground-state properties [31]. Although zero-point effects sometimes play a non-negligible role in the comparison of the ground-state properties of the proton and of the positive muon [32], in this case we are mostly concerned with the ground-state site, which is expected to be the same taking into account that the energy barriers around the site are usually larger than the zero-point energy corrections [33]. The defect calculations were performed using an 80-atom supercell with fixed lattice parameters, doubled along the  $a$ - and  $b$  axes, with periodic boundary conditions. A  $2 \times 2 \times 3$  Monkhorst-Pack  $k$ -point mesh was chosen for the Brillouin-zone integrations, with ferromagnetic alignment of the  $\text{Mn}^{3+}$  spins [34]. Effects due to spin-orbit coupling were found to be small. The final equilibrium sites of  $\text{H}^+$  were determined from energy minimization using a conjugate-gradient algorithm.

## III. EXPERIMENTAL RESULTS

### A. Zero-field measurements in the ordered magnetic phases

Representative examples of time-dependent zero-field (ZF) asymmetry, recorded at different fixed temperatures in the 2 to 50 K range, are displayed in Fig. 1. As expected, a damped oscillatory signal is observed below  $T_N = 41$  K, typical for magnetically ordered phases. However, the amplitude of the oscillations rapidly decreases on cooling towards 2 K, in such a way that the oscillations fade out after 0.015  $\mu\text{s}$ , as it can be ascertained from the data recorded below

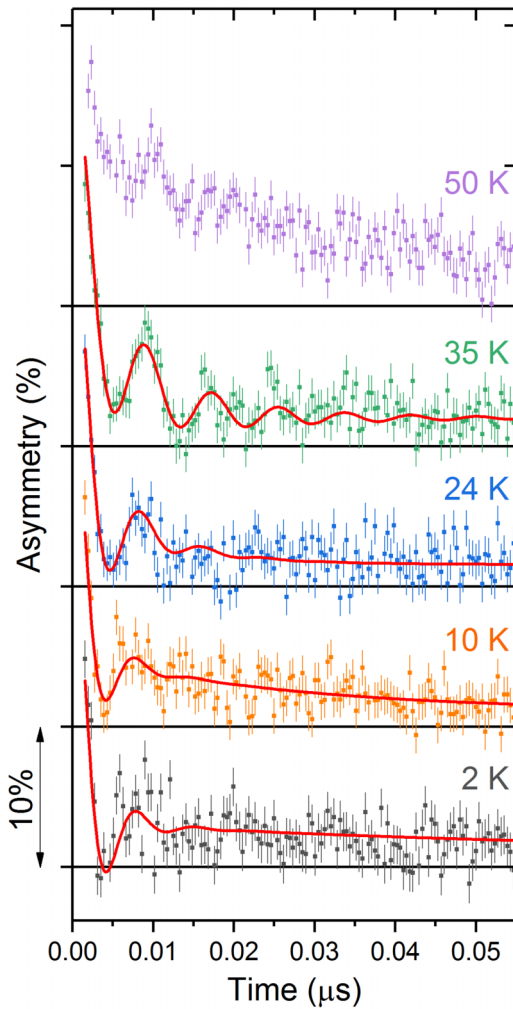


FIG. 1. Representative ZF  $\mu$ SR time-dependent asymmetry signal of  $\text{TbMnO}_3$  recorded at several fixed temperatures in 2 to 50 K range. Solid lines were determined from best fit of Eq. (1) to experimental data. Horizontal gray lines mark baseline for each temperature.

10 K. This result points to a very wide distribution of the local magnetic field that becomes wider as the temperature decreases, as expected from the coexistence of both cycloidal modulated spin structures and  $\text{Tb}^{3+}$  spins quasi-long-range ordering, below 7 K [5]. This interpretation is supported by the appearance of a diffuse neutron-scattering signal, which superimposes the magnetic diffraction satellite peak of the  $\text{Mn}^{3+}$  spin-modulated structure, as temperature approaches 7 K [35].

The time-dependent asymmetry  $A(t)$  recorded in the collinear sinusoidal incommensurate antiferromagnetic phase can be described in the  $t \leq 0.05$  –  $\mu\text{s}$  time interval by Eq. (1) [36]:

$$A(t) = A_1 e^{-\lambda_1 t} j_0(2\pi f_1 t) + A_2 e^{-\lambda_2 t}, \quad (1)$$

where  $j_0$  is the zero-order Bessel function,  $f_1 = \gamma_\mu B_\mu / 2\pi$  is the muon-spin precession frequency associated with the cutoff field,  $B_\mu$ , of the sinusoidal distribution of the internal magnetic field at the muon site,  $\gamma_\mu$  is the muon gyromagnetic ratio,  $A_{1,2}$  are the asymmetries, and  $\lambda_{1,2}$  are the relaxation rates.

The first term in Eq. (1) accounts for the relaxed oscillating component, as expected for a spatially collinear modulated spin structure, with an additional relaxation  $\lambda_1$ . This term is suitable to describe the ZF  $\mu$ SR data in the  $T_c = 28 \text{ K} \leq T \leq T_N = 41 \text{ K}$  range. However, we have kept this model to analyze all collected data because the time-dependent signal does not show significant changes that require a modification of the model in the other magnetically ordered phases. The model modification also could introduce meaningless physical temperature variations of the fitting parameters. The second term in Eq. (1) describes a spin relaxation  $\lambda_2$  of the nonoscillating component.  $\lambda_2$  has a dynamical character, which is bound to affect as well the oscillating component of the signal. Its presence indicates the influence of spin fluctuations in the ordered phases of the  $\text{Mn}^{3+}$  spins, both in the collinear sinusoidal incommensurate phase ( $T_c < T < T_N$ ) and in the cycloidal phase below  $T_c$ . The solid lines in Fig. 1 were determined by the best fit of Eq. (1) to the experimental data for  $t \leq 0.05$   $\mu\text{s}$ . The recorded spectra are well described by Eq. (1), except for the extreme cases at  $T = 2$  and 50 K. For the former case, as the data in Fig. 1 illustrate, the extremely high value of the relaxation implies that the definition of the muon-spin precession parameters becomes correspondingly difficult; higher frequencies may be present as well, but a clear separation is not possible with the present data. For the latter case, above  $T_N = 41 \text{ K}$ , we chose not to present the fit in order to call the reader's attention to that the model of Eq. (1) is not expected to be physically adequate at this temperature. The structural characterization by x-ray diffraction and Raman-scattering spectroscopy of the  $\text{TbMnO}_3$  sample used in this work, do not detect any spurious phases, precluding that these oscillations observed at 50 K arise from magnetic impurities. In fact,  $\mu$ SR experiment at 200 K (for calibration purposes) does not reveal any oscillations (see Fig. S2 of Supplemental Material [19]). Previous neutron-scattering experiments excluded the existence of long-range magnetic ordering just above  $T_N$ . Thus, the nature of the oscillations potentially observed just above the Néel temperature may be associated with correlated regions in the samples, with low spin dynamics, but the present data do now allow to clarify this question. This interpretation is supported by the experimental evidence of a spin-phonon coupling observed in  $\text{TbMnO}_3$  just below 100 K, ascertained by THz absorption spectroscopy [12]. The temperature dependence of the parameters determined from the fitting procedure is presented in Fig. 2.

From the fitting procedure, only one oscillating component could be observed; the temperature dependence of the precession frequency is shown in Fig. 2(a). The dashed line in Fig. 2(a) is a guide for the eyes. With the exception of the point at 2 K, where the fitting procedure is most difficult due to the extreme value of the spin relaxation, the spin precession frequency  $f_1(T)$  monotonously decreases on heating up to  $T_N$ , with no anomalies observed at  $T_c$ . The low-temperature value of the oscillation frequency corresponds to a local field, found to be  $B_{\text{int}} = 0.161 \text{ T}$ . The local internal field does not vanish on approaching  $T_N$  from below, as a value of 0.135 T is found close to  $T_N$ . Moreover, nonvanishing oscillations are still observed at 50 K, 9 K above  $T_N$  (cf. Fig. 1). These results contrast with the ones reported for  $\text{LaMnO}_3$ , for which two oscillating components are found in the  $\mu$ SR time-dependent

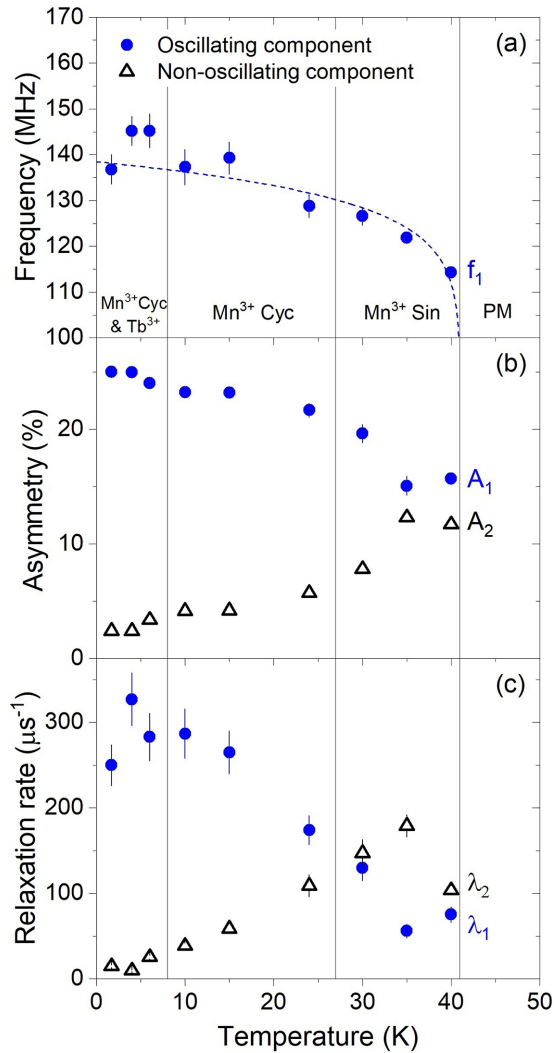


FIG. 2. Temperature dependence of (a) precession frequency, (b) asymmetries, and (c) relaxation rates, obtained from best fit of Eq. (1) to experimental data. Vertical lines mark transition temperatures between paramagnetic (PM),  $\text{Mn}^{3+}$  sinusoidal (sin), and cycloidal (cyc), and  $\text{Tb}^{3+}$  spin-ordered phases. Dashed line in (a) is guide to eyes.

asymmetry in  $\text{LaMnO}_3$  below  $T_N$  (one with similar value as that we obtained for  $\text{TbMnO}_3$ ) and both spin precession frequency and asymmetry vanish at  $T_N = 139$  K [37].

The asymmetry of the oscillating component ( $A_1$ ) increases as temperature decreases, with the asymmetry of the nonoscillating component ( $A_2$ ) decreasing, since the total asymmetry ( $A_1 + A_2$ ) was fixed constant during the fit. The amplitude of the oscillating signal depends on the angle between the local magnetic field and the muon spin. The gradual increasing of the asymmetry of the oscillating component as temperature decreases below  $T_N$  evidences that the local field direction at the muon-stopping site changes from one magnetic phase to the other.

Regarding the relaxation rates, we note that within the experimental errors, associated with the difficult fitting of Eq. (1) to the extremely damped time spectra of Fig. 1, both the dynamical relaxation  $\lambda_2$  and the relaxation  $\lambda_1$  associ-

ated with the oscillating component are comparable in the collinear sinusoidal incommensurate phase ( $T_c < T < T_N$ ). On cooling below  $T_c$ , the relaxation rate  $\lambda_2$  and the asymmetry associated with the nonoscillating component of the time-dependent  $\mu\text{SR}$  signal decrease, pointing out a slowing down of the spin-fluctuation rate with decreasing temperature, becoming nearly negligible below the ordering temperature of the  $\text{Tb}^{3+}$  spins. On the contrary, the relaxation rate  $\lambda_1$  of the oscillating component and its asymmetry increase on cooling,  $\lambda_1$  saturating at around  $300 \mu\text{s}^{-1}$  in the  $\text{Tb}^{3+}$  ordered phase, below  $T_{N2} = 7$  K. Below this temperature, the  $\lambda_1$  relaxation now includes the additional static broadening of the internal magnetic field at the muon site. In the framework of the model expressed by Eq. (1), the combination of the  $\lambda_1$  relaxation with the maximum cutoff frequency  $f_1$  indicates a maximum internal magnetic field around 3 T. The simple deviation of the cycloidal order with respect to the sinusoidal incommensurate and collinear spin ordering is not sufficient to explain the increase of the relaxation  $\lambda_1$  of the oscillating component, which we, therefore, assign to the ill-ordered  $\text{Tb}^{3+}$  spins under the influence of the magnetic field of the  $\text{Mn}^{3+}$  spin sublattice. This interpretation is based on the observation of a diffuse neutron-scattering signal, better observed below 12 K in the neighborhood of the satellite peak associated with the modulated  $\text{Mn}^{3+}$  spin structure [35]. This result, along with the increasing trend of  $\lambda_1$  on cooling, points to an increasingly wider distribution of the local magnetic field and disorder induced by the  $\text{Tb}^{3+}$  spins.

## B. Transverse field measurements above $T_N$

In this section, we will report the results of the temperature-dependent transverse magnetic field (TF)  $\mu\text{SR}$  experiments from 10 to 300 K, the external magnetic field applied along the  $b$  axis. The spectral components in the measured signal were obtained by the corresponding Fourier transforms from the analysis using the MUSRIT software [20], and are presented in Fig. 3, for the highest (8-T) magnetic-field strength, as a representative result. The Fourier transforms for 1-, 3-, 5-, and 6.5-T magnetic-field strengths can be found in Fig. S3 of Supplemental Material [19].

A prominent spectral component is always observed in the entire temperature/magnetic-field ranges, peaking near the muon Larmor frequency, associated with the applied magnetic field. The nominal Larmor frequency is marked in Fig. 3 by the vertical solid line. The Fourier transform of the time-dependent TF  $\mu\text{SR}$  signal reveals the existence of other spectral components that can be grouped into two main sets: one at frequencies close to the Larmor frequency, and another set at lower frequencies. The existence of different spectral components in the time-dependent TF  $\mu\text{SR}$  signal evidences for different muon-stopping sites, which probe different local magnetic fields strengths. The set of frequencies close to the Larmor frequency includes a small contribution from muons stopping in the silver sample holder. This set likely includes as well a distribution of frequencies associated with muons stopping in slightly magnetically inequivalent sites, but our data do not allow a clear separation of these components among themselves or of the silver contribution. The description of this complex shape is not straightforward



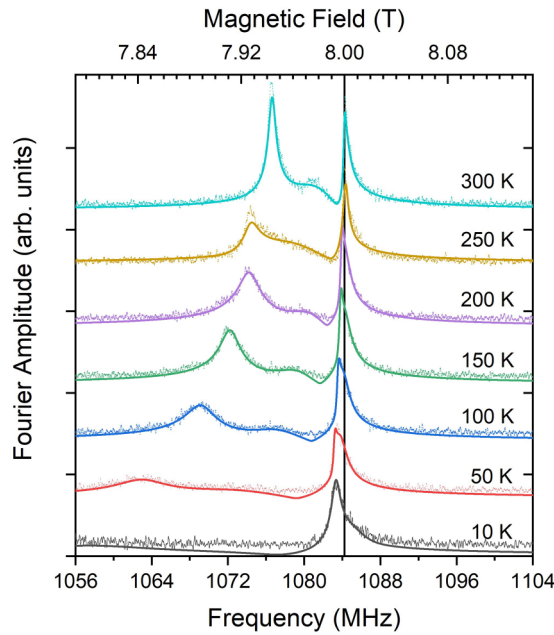


FIG. 3. Representative Fourier transform of time-dependent TF  $\mu$ SR signal of  $\text{TbMnO}_3$ , with corresponding best fits, recorded at several fixed temperatures in 10 to 300 K range, with applied transverse magnetic field of 8 T, applied along  $b$  axis. Vertical gray line marks corresponding nominal gyromagnetic frequency.

and several fitting schemes were tried; we finally found that this spectral distribution around the Larmor frequency is described in a reasonable way for all temperatures and fields by a Lorentzian-damped oscillation, which essentially describes a rather temperature-independent contribution (including that of the muons stopping in the silver sample holder) and a Gaussian-damped oscillation which describes a contribution with a slight temperature dependence. As we will discuss below, this work is not focused on these components, but rather on the spectral weight shifted to lower frequencies, which captures clearly the temperature dependence of the observed Knight shift.

The spectral components found at frequencies significantly shifted to values much lower than the Larmor frequency also include at least two distinct components, which are rather broad in the fast Fourier transform spectra, shown in Fig. 3. This is basically described by two components with a Gaussian relaxation. As the temperature decreases from 300 K, these two peaks are observed to shift to lower frequencies and progressively broader up to 50 K (also deviating from the Gaussian shape). Below 50 K, well within the ordered magnetic phases, it is still possible (although very difficult) to fit this low-frequency part with two highly shifted broad peaks, which qualitatively corroborate the broader local magnetic-field distribution associated with the modulated spins structures and the  $\text{Tb}^{3+}$  spin ill-ordering. The relaxation rates at 10 K are of the order of tens of  $\mu\text{s}^{-1}$ ; this is about the same order of magnitude as that of the nonoscillatory component in ZF measurements, which was assigned to a dynamical relaxation. The fit curves at  $T = 10$  K should nevertheless be considered as a mere suggestion, since the magnetic-field distribution within the magnetically ordered phase is clearly

not captured by the fitting model used for the paramagnetic phase.

The time-dependent TF  $\mu$ SR signal was therefore fitted with four oscillating components using the MUSRFIT software: two Gaussian relaxing describing the low-frequency part and a set of a Gaussian relaxing and a Lorentzian relaxing describing the high-frequency peaks around the Larmor frequency. The analysis reveals no significant variations of the two components at higher frequency, as well as of the relative oscillating amplitudes and phases. This fitting scheme captures the essential behavior of the overall temperature and field dependence of our data and reveals a significant dependence with temperature of the frequencies and relaxation of the two components at lower frequency. For the highest fields ( $B = 6.5$  and 8 T), a mismatch between the fit curve and the data is evident just below the high-frequency peaks for  $T \leq 200$  K, being more pronounced at 10 K. This mismatch at 10 K corroborates the magnetic field-induced effects on the magnetic structure leading to the reorientation of the spin cycloid from the  $bc$  plane to the  $ac$  plane and the polarization flop observed for  $B \geq 5$  T at 10 K [4], likely associated with the Tb momenta, which changes the shape of the local field distribution at the muon site(s) [7]. The cases between 50 and 200 K will be addressed later on. Figure 4 shows the temperature dependence of the frequency and relaxation rate of each component for the representative case of 8 T (the corresponding parameters calculated for the remaining data recorded at other applied magnetic fields may be found in Fig. S4 of Supplemental Material [19]).

We therefore focus our analysis on the lower-frequency components (blue triangles and green circles in Figs. 4 and S4 of Supplemental Material [19]). The negative frequency shifts from the nominal value of the Larmor frequency as temperature decreases are attributed to the increase of the local magnetic susceptibility, as discussed below, whereas the increase of the relaxation rate points to a less homogeneous magnetic-field distribution in the sample at lower temperatures or different spin dynamics.

In the paramagnetic phase, a shift of the muon frequency is usually observed, because the local magnetic field is different from the applied one. This is defined as the experimental Knight shift  $K^{\text{exp}}$ , expressed as [38]

$$K^{\text{exp}} = \frac{\vec{B}_{\text{ext}} \cdot (\vec{B}_{\text{loc}} - \vec{B}_{\text{ext}})}{B_{\text{ext}}^2} = \frac{(B_{\text{loc}} - B_{\text{ext}})}{B_{\text{ext}}} = \frac{2\pi \frac{f}{\gamma} - B_{\text{ext}}}{B_{\text{ext}}}, \quad (2)$$

where  $B_{\text{ext}}$  is the applied magnetic-field strength,  $B_{\text{loc}}$  is the local magnetic field at the muon position, calculated from the frequency ( $f$ ) divided by the muon gyromagnetic ratio ( $\gamma$ ). As discussed above, the high-frequency components include a contribution from muons stopping in the silver sample holder and precessing (within the very small diamagnetic shift in silver, of the order of a few ppm) at the muon Larmor frequency. We cannot clearly separate the silver component and therefore used the frequency of the Gaussian-relaxing component (red triangles in Fig. 4) as the reference for  $B_{\text{ext}}$ ; this may introduce a systematic error in the calculation of the corresponding Knight shift, leading to a vertical displacement that is estimated to be smaller than 0.1%. The Knight shift is

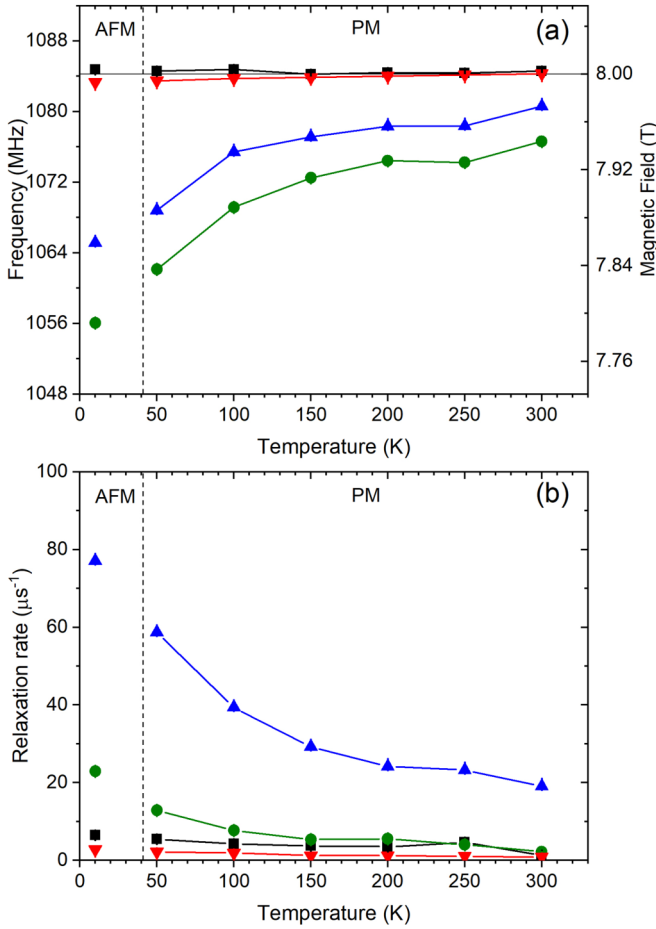


FIG. 4. (a) Frequency and (b) relaxation-rate temperature dependence of oscillating components obtained from fit to time-dependent  $\mu$ SR signal of  $\text{TbMnO}_3$  recorded for magnetic field of 8 T, respectively, applied along  $b$  axis. Vertical dashed lines mark Néel temperature  $T_N$ . Gaussian shape of relaxation was adopted for all components except for component indicated with black squares (where Lorentzian shape was adopted).

very significant for the lower-frequency components, which are strongly temperature dependent and therefore present a larger negative Knight shift, as can be observed in Fig. S5 of Supplemental Material [19]. As we will discuss below, the S-shaped anomaly of the  $K^{\text{exp}}(T)$  curve obtained for these two components resembles the anomalous temperature behavior of the magnetic susceptibility  $\chi_b(T)$ . As observed for the  $\chi_b^{-1}(T)$  curve, a linear temperature dependence of  $K^{\text{exp}}(T)$  is found in the 150 to 300 K range, with a clear deviation below 150 K (see Fig. S5 of Supplemental Material [19]).

In the paramagnetic phase of an insulating oxide, the muon Knight shift should scale with the magnetic susceptibility, as follows [38]:

$$K_b^\mu = K^{\text{exp}} - \left(\frac{1}{3} - N\right)\chi_b, \quad (3)$$

where  $(\frac{1}{3} - N)\chi_b$  is the correction accounting for the Lorentz and demagnetization fields,  $N$  is the demagnetization ratio, and  $\chi_b$  is the bulk magnetic susceptibility, measured along the  $b$  axis. The  $N$  value was estimated from the sample dimensions assuming a parallelogrammatical shape, with the table

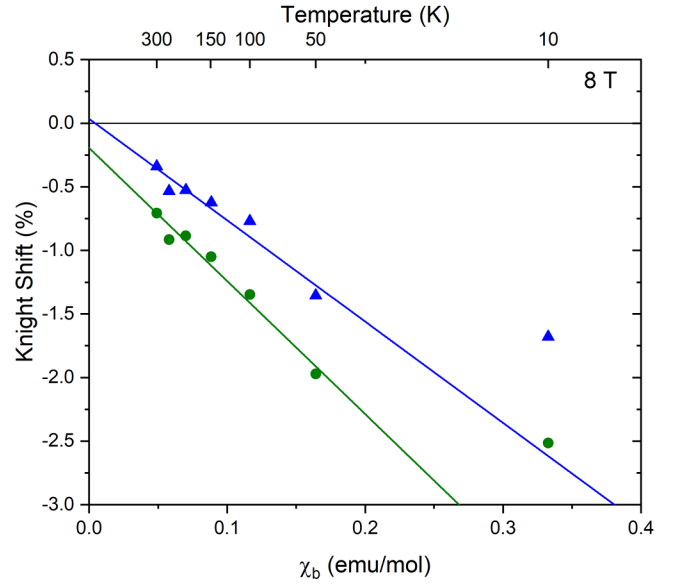


FIG. 5. Muon Knight shift calculated from oscillation frequency of lower-frequency components (as discussed in text) as function of  $\chi_b$  component of susceptibility tensor of  $\text{TbMnO}_3$  for 8 T of applied transverse magnetic field along  $b$  axis.

presented in Ref. [39], resulting in  $N \approx 0.2$ . On the other hand, the Knight shift is a consequence of both the dipolar field of localized magnetic momenta, associated with the Mn 3d and Tb 4f electrons, and the contact field, due to the field-induced magnetic polarization of the local moments.

Following the current literature, when the magnetic field is applied along the  $b$  axis, we have [38]

$$K_b^\mu(T) = (\mathcal{D}_{\vec{r}_\mu}^{bb} + A_{\text{cont},fd,\vec{r}_\mu})\chi_b(T), \quad (4)$$

where  $\mathcal{D}_{\vec{r}_\mu}^{bb}$  is the  $bb$  ( $yy$ ) diagonal dipolar and  $A_{\text{cont},fd,\vec{r}_\mu}$  is the contact tensor elements, both measured at the muon site  $\vec{r}_\mu$ . Figure 5 shows the muon Knight shift as a function of the  $\chi_b$  component of the magnetic susceptibility tensor, obtained from the experimental values of the two lower-frequency components at 8 T (see Fig. S6 of Supplemental Material for 1, 3, 5, and 6.5 T [19]). Remarkably, despite both the muon Knight shift and the inverse bulk magnetic anomalies presenting deviations from linearity in their temperature dependences (for temperatures below 150 K, as shown in Fig. S2 and in the S-shaped anomaly in Fig. S5), the linear dependence of the muon Knight shift as a function of the bulk magnetic susceptibility is observed for both components in the entire temperature range down to 50 K, above  $T_N = 41$  K (Fig. 5). This means that the local and macroscopic magnetic susceptibilities exhibit the same temperature behavior, within experimental error, in the 50–300 K range. Consequently, this result clearly rules out the existence of any short-range magnetic ordering well above  $T_N$ , as it has been assumed to be present in the  $T_N < T < 150$  K [13]. If it existed, it would change the local magnetic susceptibility and the linearity between Knight shift and macroscopic magnetic susceptibility would not occur. This is evident for the data points at 10 K, where the fully developed magnetic ordering at that

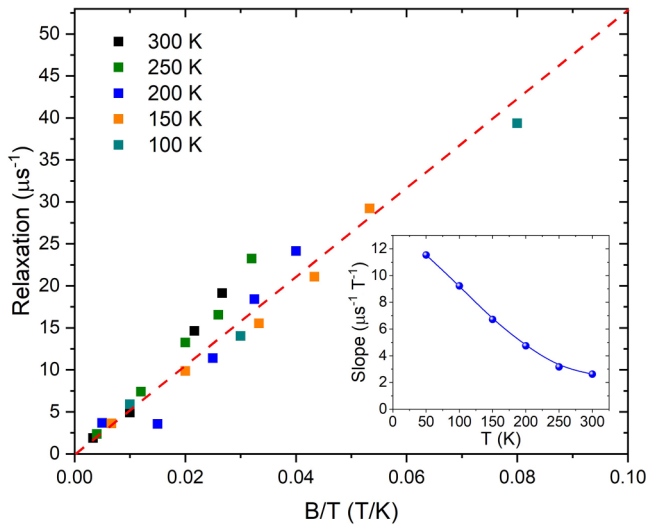


FIG. 6. Relaxation rate of highest relaxing component as function of applied magnetic-field strength divided by corresponding temperature. We used relaxation values of highest relaxation component (represented as blue triangles in Figs. 4 and S4 of Supplemental material [19]). Dashed line is guide for eyes. Inset: Temperature dependence of linear slope obtained from best linear fit of relaxation rate value (300 to 150 K) against applied magnetic-field strength.

temperature causes it to be clearly deviated from the linearity found between 50 and 300 K.

This interpretation is fully corroborated by the analysis of the effect of the applied magnetic field on the relaxation-rate value of the muon precession signal. To get more reliable results, we chose to analyze the data concerning the spectral component with the highest relaxation value (blue triangles in Figs. 4(b) and S4 of the Supplemental Material [19]). In the paramagnetic phase, the muon relaxation rate is expected to be proportional to the net induced macroscopic magnetization by the external field which, in turn, is proportional to the  $B/T$  ratio [40]. The unique linear relationship found between the relaxation rate values and  $B/T$ , between 100 and 300 K, depicted in Fig. 6, definitively excludes the existence of short-range magnetic interactions above 100 K, contrary to what has been assumed before [13]. At 50 K, a slight deviation already occurs (not shown), most likely associated with the precursor effects already discussed in the zero-field  $\mu$ SR data (cf. Fig. 1). Further confirmation comes from the lack of anomalous temperature behavior of the slopes obtained from the best linear fit between relaxation value and applied magnetic field, for each temperature between 150 and 300 K, shown in the inset of Fig. 6 (the linear fits are shown in Fig. S7 of Supplemental Material [19]). So, we conclude that  $\text{TbMnO}_3$  behaves as a usual paramagnet above 50 K.

#### IV. UNUSUAL MAGNETOSTRUCTURAL COUPLING IN PARAMAGNETIC PHASE

DFT calculations were performed to obtain the theoretically predicted stable muon-stopping sites, in order to contribute to the interpretation of the experimental data. The obtained minimum-energy configurations after structural relaxation are shown in Fig. 7, which depicts the nearest

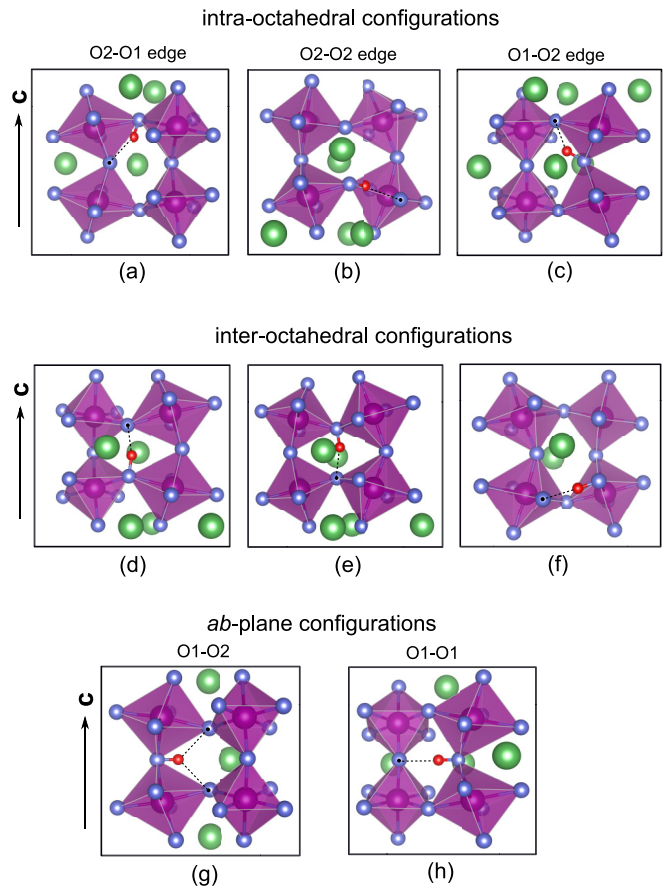


FIG. 7. Atomistic structures of all minimum-energy  $\text{H}^+$  configurations. Dashed lines connect  $\text{H}^+$  to their next-nearest neighbor oxygen ions, ONNN. The  $\text{H}^+$ ,  $\text{O}^{2-}$ , and  $\text{Tb}^{3+}$  are depicted by red, blue, and large green spheres, respectively, with  $\text{Mn}^{3+}$  at  $\text{MnO}_6$  octahedra centers. View is perpendicular to crystallographic  $c$  axis, with being O1 apical oxygens and O2 basal ones.

corner-sharing  $\text{MnO}_6$  octahedra. The introduction of the  $\text{H}^+$  nuclei in the host lattice did not lead to any breaking of Mn–O bonds. For all distinct muon sites, there is a strong tendency to bind to oxygen ions of the lattice, with the formation of a short O–H bond with length about 1.0 Å. The next-nearest oxygen neighbors are also depicted by the dashed lines. In contrast, all muon-stopping sites were found to be at least 2.0 Å away from the nearest  $\text{Mn}^{3+}$  and  $\text{Tb}^{3+}$  ions, a finding that very likely originates from the electrostatic repulsion with these positively charged ions. We ascertained that for all the possibilities the muon in  $\text{TbMnO}_3$  is always located near the oxygen ions. This is in good agreement with the stable muon-stopping sites in the structurally homologous rare-earth orthoferrites ( $\text{RFeO}_3$ ), where the formation of the hydroxyl O–H bond was also inferred [31]. See Supplemental Material for more information [19]. It is also important to clarify here that the different zero-point energy (ZPE) between the proton and the muon may lead to some different behavior since the muon is capable of accessing larger regions around its equilibrium site by local vibrations, owing to its smaller mass. The magnitude of ZPE, however, for either particle will not modify the site identification presented here and both particles will remain localized at the determined sites. Furthermore, it is very

unlikely that the muon can access its high-amplitude vibrational states for the low and moderate temperatures treated in this work. In fact, earlier DFT-based calculations in perovskite type and other oxides reported ZPE corrections for proton migration equal to 0.12 eV [33,41]. Assuming a harmonic approximation by taking into account the different isotopic mass ( $m\mu = 0.113$  mp) this translates to about 0.36 eV for the ZPE of the muon. Nonetheless, activation energies of proton diffusion from conductivity measurements in classes of doped perovskite-type oxides that are known proton conductors were reported to be within a range from 0.43 to 0.50 eV [42]. For  $\text{TbMnO}_3$  these energies should be expected to be even higher. Therefore, albeit large, the ZPE of the muon is not large enough to lead to migration and site changes.

In the previous section, we concluded that the mechanism responsible for the abnormal temperature dependence of both magnetic susceptibility and Knight shift cannot be ascribed to magnetic correlations above 50 K. As it was referred to above, many physical quantities exhibit abnormal temperature dependence below 200 K, still in the paramagnetic phase. Figure S8 of Supplemental Material [19] depicts a collection of such results from the literature, involving thermal expansion [10], magnetization [7], and electromagnon oscillator strength [13] occurring in  $\text{TbMnO}_3$ . The results unequivocally ascertain a magnetoelastic coupling in the paramagnetic phase of this material. Detailed temperature-dependent infrared spectroscopy has shown that the wave number and oscillator strength of polar phonons assigned to  $\text{MnO}_6$  octahedra exhibit anomalies at around 200 K [8,12]. These internal polar vibrations involve both Mn–O and O–Mn–O bond vibrations, and evidence for octahedral distortions occurring in this temperature range [8,12]. Following this idea, the oxygen position shift would change the electronic orbital overlapping and, consequently, the superexchange integral values, as demonstrated both theoretically and experimentally [43,44]. Although the mechanism underlying the lattice distortion is still unknown, the octahedra distortion will promote the changes in the local magnetic properties. From our DFT calculations showing that in all the muon-stopping sites, the muon lies preferentially much closer to the oxygen ions, we interpret that the oxygen shift below 200 K affects the local magnetic field at the muon-stopping sites, causing the S-shaped curvature of the Knight shift versus temperature. This fully explains our results, with no short-range magnetic ordering being necessary. Regarding the mismatch between the fit curve and the data for the highest magnetic fields ( $B = 6.5$  and 8 T), between 50 and 200 K, observed in Fig. 3 and Fig S3 of the Supplemental Material [19], we must not exclude that the magnetoelastic coupling

here evidenced may be responsible for this mismatch between experimental data and the simple model used to describe it.

## V. CONCLUSIONS

In this work, we were able to ascertain the extremely broad distribution of the local magnetic field in  $\text{TbMnO}_3$  at low temperatures, from the high relaxation rate observed in the muon spin oscillations at zero-field. A local magnetic field of 0.161 T was extracted at low temperatures, but the width of the distribution was estimated to be much higher and the maximum internal field was estimated at about 3 T. This wide distribution of the local magnetic field arises from both from the modulated spin orderings of the  $\text{Mn}^{3+}$  and from the quasi-long-range ordering of the  $\text{Tb}^{3+}$  spins.

The experiments under applied transverse magnetic field up to room temperature show that although the Knight shift expected from the paramagnetic phase has an anomaly with temperature around 150 K, it scales linearly with the magnetic susceptibility, which shows an anomaly at the same temperature. Moreover, the relaxation rate also scales linearly between 100 and 300 K with  $B/T$ . This indicates that  $\text{TbMnO}_3$  remains purely paramagnetic at these temperatures, with the magnetic susceptibility being the same macroscopically and at a local length scale. We are thus allowed to conclude that a shift of the oxygen positions, to which the muon is attached, and concomitant effect on the  $\text{Tb}^{3+}$  crystal-field levels, produces all the experimental anomalies reported in this temperature range by different characterization techniques, namely changing the magnetic susceptibility via magnetoelastic effect.

## ACKNOWLEDGMENTS

We are deeply indebted to Robert Scheuermann for his valuable assistance and fruitful advice during the analysis of experimental results and the writing of this manuscript. We also acknowledge the Swiss Muon Source (S $\mu$ S), Paul Scherrer Institute, Villigen, Switzerland for beam time allocation and the technical support of the PSI muon team. This work was supported with funds from Grants No. NORTE-01-0145-FEDER-022096, No. UIDB/04968/2020, No. UIDB/04564/2020, No. UIDP/04564/2020, No. PTDC/NAN-MAT/28538/2017, and No. PTDC/FIS/03564/2022, and SAS VEGA 2/0011/22 projects, Scientific Grant Agency MŠVVaŠ SR and SAS Project No. VEGA 2/0011/22 and R.V. from Grant No. PTDC/NAN-MAT/0098/2020.

[1] T. Kimura, T. Goto, H. Shintani, K. Ishizaka, T. Arima, and Y. Tokura, *Nature (London)* **426**, 55 (2003).  
 [2] T. Goto, T. Kimura, G. Lawes, A. P. Ramirez, and Y. Tokura, *Phys. Rev. Lett.* **92**, 257201 (2004).  
 [3] T. Goto, Y. Yamasaki, H. Watanabe, T. Kimura, and Y. Tokura, *Phys. Rev. B* **72**, 220403(R) (2005).  
 [4] T. Kimura, G. Lawes, T. Goto, Y. Tokura, and A. P. Ramirez, *Phys. Rev. B* **71**, 224425 (2005).

[5] R. Kajimoto, H. Yoshizawa, H. Shintani, T. Kimura, and Y. Tokura, *Phys. Rev. B* **70**, 012401 (2004).  
 [6] T. Kimura, S. Ishihara, H. Shintani, T. Arima, K. T. Takahashi, K. Ishizaka, and Y. Tokura, *Phys. Rev. B* **68**, 060403(R) (2003).  
 [7] D. O'Flynn, M. R. Lees, and G. Balakrishnan, *J. Phys.: Condens. Matter* **26**, 256002 (2014).



- [8] S. Mansouri, S. Jandl, M. Balli, P. Fournier, A. A. Mukhin, V. Y. Ivanov, A. Balbashov, and M. Orlita, *J. Phys.: Condens. Matter* **30**, 175602 (2018).
- [9] K. Berggold, J. Baier, D. Meier, J. A. Mydosh, T. Lorenz, J. Hemberger, A. Balbashov, N. Aliouane, and D. N. Argyriou, *Phys. Rev. B* **76**, 094418 (2007).
- [10] J. Blasco, C. Ritter, J. García, J. M. de Teresa, J. Pérez-Cacho, and M. R. Ibarra, *Phys. Rev. B* **62**, 5609 (2000).
- [11] M. A. Carpenter, D. Pesquera, D. O'Flynn, G. Balakrishnan, N. Mufti, A. A. Nugroho, T. T. M. Palstra, M. Mihalik Jr., M. Mihalik, M. Zentková, A. Almeida, J. A. Moreira, R. Vilarinho, and D. Meier, *J. Phys.: Condens. Matter* **33**, 125402 (2021).
- [12] A. Maia, R. Vilarinho, C. Kadlec, M. Lebeda, M. Mihalik, M. Zentková, M. Mihalik, J. A. Moreira, and S. Kamba, *Phys. Rev. B* **107**, 104410 (2023).
- [13] Y. Takahashi, N. Kida, Y. Yamasaki, J. Fujioka, T. Arima, R. Shimano, S. Miyahara, M. Mochizuki, N. Furukawa, and Y. Tokura, *Phys. Rev. Lett.* **101**, 187201 (2008).
- [14] D. S. Andrievskii, S. I. Vorob'ev, A. L. Getalov, E. I. Golovenchits, E. N. Komarov, S. A. Kotov, V. A. Sanina, and G. V. Shcherbakov, *JETP Lett.* **106**, 295 (2017).
- [15] P. Hohenberg and W. Kohn, *Phys. Rev.* **136**, B864 (1964).
- [16] W. Kohn and L. J. Sham, *Phys. Rev.* **140**, A1133 (1965).
- [17] M. Mihalik, M. Mihalik, Z. Jagličić, R. Vilarinho, J. A. Moreira, E. Queiros, P. B. Tavares, A. Almeida, and M. Zentková, *Phys. B: Condens. Matter* **506**, 163 (2017).
- [18] M. Mihalik, M. Zentková, A. Maia, R. Vilarinho, A. Almeida, J. Agostinho Moreira, J. Pospíšil, and K. Uhlířová, *J. Magn. Magn. Mater.* **549**, 168986 (2022).
- [19] See Supplemental Material at <http://link.aps.org/supplemental/10.1103/PhysRevB.108.174401> for specific-heat and magnetic susceptibility data confirming expected phase transitions; complementary muon spectroscopy data; temperature anomalies of lattice parameters, magnetization, and electromagnon oscillator strength taken from literature; and details of DFT calculations.
- [20] A. Suter and B. M. Wojek, *Phys. Proc.* **30**, 69 (2012).
- [21] F. L. Pratt, *Phys. B: Condens. Matter* **289–290**, 710 (2000).
- [22] G. Kresse and J. Hafner, *Phys. Rev. B* **47**, 558 (1993).
- [23] G. Kresse and J. Furthmüller, *Comput. Mater. Sci.* **6**, 15 (1996).
- [24] G. Kresse and J. Furthmüller, *Phys. Rev. B* **54**, 11169 (1996).
- [25] S. L. Dudarev, G. A. Botton, S. Y. Savrasov, C. J. Humphreys, and A. P. Sutton, *Phys. Rev. B* **57**, 1505 (1998).
- [26] H. J. Xiang, S.-H. Wei, M.-H. Whangbo, and J. L. F. Da Silva, *Phys. Rev. Lett.* **101**, 037209 (2008).
- [27] N. S. Fedorova, C. Ederer, N. A. Spaldin, and A. Scaramucci, *Phys. Rev. B* **91**, 165122 (2015).
- [28] V. Sharma, A. McDannald, M. Staruch, R. Ramprasad, and M. Jain, *Appl. Phys. Lett.* **107**, 012901 (2015).
- [29] G. Kresse and D. Joubert, *Phys. Rev. B* **59**, 1758 (1999).
- [30] J. P. Perdew, K. Burke, and M. Ernzerhof, *Phys. Rev. Lett.* **77**, 3865 (1996).
- [31] E. Holzschuh, A. B. Denison, W. Kündig, P. F. Meier, and B. D. Patterson, *Phys. Rev. B* **27**, 5294 (1983).
- [32] M. Gomilšek, F. L. Pratt, S. P. Cottrell, S. J. Clark, and T. Lancaster, *Commun. Phys.* **6**, 142 (2023).
- [33] A. G. Marinopoulos, R. C. Vilão, H. V. Alberto, and J. M. Gil, *J. Phys.: Condens. Matter* **30**, 425503 (2018).
- [34] H. J. Monkhorst and J. D. Pack, *Phys. Rev. B* **13**, 5188 (1976).
- [35] A. Maia, R. Vilarinho, P. Proschek, M. M. Jr., M. Zentková, M. Mihalik, M. Lebeda, S. Kamba, and J. A. Moreira (unpublished).
- [36] I. Yamauchi, M. Hiraishi, H. Okabe, S. Takeshita, A. Koda, K. M. Kojima, R. Kadono, and H. Tanaka, *Phys. Rev. B* **97**, 134410 (2018).
- [37] M. C. Guidi, G. Allodi, R. De Renzi, G. Guidi, M. Hennion, L. Pinsard, and A. Amato, *Phys. Rev. B* **64**, 064414 (2001).
- [38] A. Schenck, Lecture Notes on Static Magnetic Properties of Metallic Systems Explored by USR-Spectroscopy.
- [39] P. G. Akishin and I. A. Gaganov, *J. Magn. Magn. Mater.* **110**, 175 (1992).
- [40] S. Blundell, *Magnetism in Condensed Matter* (Oxford University Press, Oxford, 2001).
- [41] P. G. Sundell, M. E. Björketun, and G. Wahnström, *Phys. Rev. B* **76**, 094301 (2007).
- [42] K. D. Kreuer, S. Adams, W. Münch, A. Fuchs, U. Klock, and J. Maier, *Solid State Ionics* **145**, 295 (2001).
- [43] M. Mochizuki, N. Furukawa, and N. Nagaosa, *Phys. Rev. B* **84**, 144409 (2011).
- [44] M. Rini, R. Tobey, N. Dean, J. Itatani, Y. Tomioka, Y. Tokura, R. W. Schoenlein, and A. Cavalleri, *Nature (London)* **449**, 72 (2007).